Highly efficient beamline and spectrometer for inelastic soft X-ray scattering at high resolution

C. H. Lai,[a,b] H. S. Fung,[a] W. B. Wu,[a] H. Y. Huang,[a,b] H. W. Fu,[a] S. W. Lin,[a] S. W. Huang,[a]‡ C. C. Chiu,[a] D. J. Wang,[a] L. J. Huang,[a] T. C. Tseng,[a] S. C. Chung,[a] C. T. Chen[a] and D. J. Huang[a,b]*

[a]National Synchrotron Radiation Research Center, Hsinchu 30076, Taiwan, and [b]Department of Physics, National Tsing Hua University, Hsinchu 30013, Taiwan. *E-mail: djhuang@nsrrc.org.tw

The design, construction and commissioning of a beamline and spectrometer for inelastic soft X-ray scattering at high resolution in a highly efficient system are presented. Based on the energy-compensation principle of grating dispersion, the design of the monochromator–spectrometer system greatly enhances the efficiency of measurement of inelastic soft X-rays scattering. Comprising two bendable gratings, the set-up effectively diminishes the defocus and coma aberrations. At commissioning, this system showed results of spin-flip, d–d and charge-transfer excitations of NiO. These results are consistent with published results but exhibit improved spectral resolution and increased efficiency of measurement. The best energy resolution of the set-up in terms of full width at half-maximum is 108 meV at an incident photon energy tuned about the Ni L_3-edge.

1. Introduction

Inelastic X-ray scattering (IXS) provides direct information about elementary excitations arising from the charge fluctuations of materials. If a core electron is resonantly excited to an absorption threshold with an incident photon, the resulting emission spectrum depends strongly on the energy of those photons; IXS of this type is called 'resonant inelastic X-ray scattering' (RIXS) (Kotani & Shin, 2001; Ament et al., 2011). The resonance effect greatly enhances the scattering cross section and yields a direct probe of excitations. This spectral method is particularly promising because it reveals the electronic properties of materials with atomic specificity via a photon-in/photon-out process, and does not require an ultrahigh vacuum.

Advances in the technology of a synchrotron light source have enabled much improvement of the experimental techniques of RIXS in the soft X-ray regime, providing great scientific opportunities (Hatsui et al., 2005; Ghiringhelli et al., 2006, 2012; Tokushima et al., 2006; Agaker et al., 2009; Strocov et al., 2010; Harada et al., 2012; Schmitt et al., 2013). The spectral resolution ΔE at the Cu L_3-edge has been improved from 1.6 eV at an early stage (Ichikawa et al., 1996) to about 0.1 eV (Ghiringhelli et al., 2012; Schmitt et al., 2013). L-edge RIXS has proved effective in detecting charge, orbital and

magnetic excitations. For instance, RIXS measurements unravelled the spin–orbital separation in a quasi-one-dimensional Mott insulator (Schlappa et al., 2012). A desirable resolution of RIXS would be about 30 meV (Green, 1999), but an experiment to fulfil that resolution requires photons of great brilliance and a highly efficient monochromator or spectrometer. Fung et al. proposed a novel design for a RIXS set-up comprising two bendable gratings, termed an active-grating monochromator (AGM) or active-grating spectrometer (AGS), to enhance the efficiency of measurement of inelastic X-rays through an increased bandwidth of incident photons but without smearing the energy resolution (Fung et al., 2004).

In this article we report on the design, construction and commissioning results of a beamline and spectrometer for inelastic soft X-ray scattering at high resolution. A test beamline and spectrometer were constructed at the National Synchrotron Radiation Research Center (NSRRC), Taiwan. The design of the monochromator–spectrometer system conforms to our stated concept (Fung et al., 2004). We discuss our approach to implement the AGM–AGS scheme and the commissioning results of RIXS measurements of NiO. The best energy resolution ΔE in terms of full width at half-maximum (FWHM) is 108 meV at an incident photon energy tuned about the Ni L_3-edge. Our work experimentally demonstrates that the energy-compensation principle of grating dispersion functions for soft X-ray spectra.

research papers

2. Design of the AGM–AGS beamline and spectrometer

2.1. Active monochromator and spectrometer

The design of our monochromator and spectrometer is based on the energy-compensation principle of grating dispersion. In adopting this concept, we employed two bendable gratings with varied line spacing (VLS) such that the incident and scattered X-rays were appropriately focused onto the sample and the detector, respectively. We used active VLS gratings in the AGM–AGS design for these advantages: an active grating can vary the surface profile to match the desired energy setting, and a VLS grating design provides flexible parameters of the ruling density of the grating to cancel the coma abbreviation and the asymmetry of the spectral line shape (Strocov *et al.*, 2011). These parameters were tuned to optimize the working conditions of the AGM–AGS system.

Fig. 1 illustrates the geometric relation of the optical parameters of the grating in the dispersion plane in terms of an ω–ξ Cartesian coordinate system in which the ξ-axis is along the surface normal at the grating centre O and the profile function of the grating is $P(\omega, \xi)$. For a VLS grating, the groove density $n(\omega)$ is varied along the ω-axis as follows,

$$n(\omega) = n_0 + n_1\omega + n_2\omega^2 + \cdots, \quad (1)$$

in which n_0 is the ruling density at the grating centre and n_i ($i = 1$ to ∞) are the coefficients of varied ruling density. In the present design we retained only the linear coefficient n_1 and set the high-order coefficients to be zero. Considering a source point A, an image point B and a central ray OA that enters the VLS grating as shown in Fig. 1, the optical path difference (OPD) between the central ray AOB and the general ray APB is expressible with a power series in ω. According to Fermat's principle, the source point A becomes focused to an image point B by the grating if OPD = 0. Each coefficient in the power series of the OPD is required to be zero. For incident angle α and dispersion angle β, one minimizes the OPD to the first order of ω to deduce the grating equation as follows,
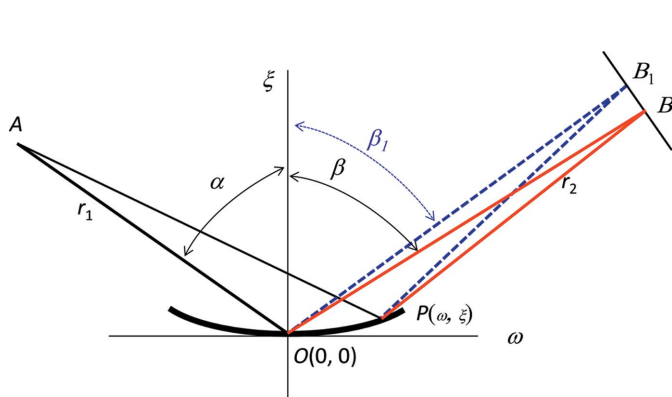
$$(\sin \alpha + \sin \beta) + kn_0\lambda = 0, \quad (2)$$

in which k and λ are, respectively, the diffraction order and the wavelength of the dispersed light. Here we adopt the notation of Fig. 1 in which α and β have opposite signs if they are on opposite sides of the grating normal. Fig. 1 illustrates also that an incident X-ray beam composed of two wavelengths λ and λ_1 is dispersed by the grating to two separate points B and B_1. The dispersion change Δy between B and B_1 along the direction perpendicular to the light propagation in the ω–ξ plane is described as follows,

$$\Delta y = \frac{kr_2 n_0}{\cos \beta} \, \Delta\lambda, \quad (3)$$

in which $\Delta\lambda = \lambda_1 - \lambda$ is the deviation in wavelength.

For a grating surface of profile $\xi = a_2\omega^2 + a_3\omega^3$, the minimization of the OPD to the second order of ω yields

$$(\cos \alpha + \cos \beta)\, a_2 = \frac{1}{2}\left(-kn_1\lambda + \frac{\cos^2 \alpha}{r_1} + \frac{\cos^2 \beta}{r_2}\right). \quad (4)$$

In a spherical-grating monochromator (SGM), the major optical aberrations that limit the spectral resolution are defocus and coma aberrations. As the photon energy varies, the exit slit of the SGM must be moved to an appropriate position to eliminate the defocus aberration. An altered grating radius can alternatively serve the purpose of eliminating the defocus aberration. As the surface profile of the grating is bendable, coefficients a_2 and a_3 are adjustable to reduce effectively the defocus and coma aberrations, respectively, so as to optimize the spectral resolution.

2.2. The energy-compensation principle

Fig. 2 shows the optical arrangement of a monochromator–spectrometer design based on the energy-compensation principle of grating dispersion for inelastic X-ray scattering. Incident X-rays from an entrance slit are focused and dispersed by an AGM of an entrance arm r_1 and an exit arm r_2 onto a sample with energy bandwidth 2ε. Scattered X-rays are focused and dispersed onto a detector by an AGS that has an

Figure 1
Optical parameters of a VLS active grating. $P(\omega, \xi)$ is a general point on the grating surface in the ω–ξ plane. A is the source point and O is the grating centre. OA is the central ray entering the VLS grating. B and B_1 are image points of varied energies. r_1 and r_2 are distances from the grating to the source and the image point, respectively.
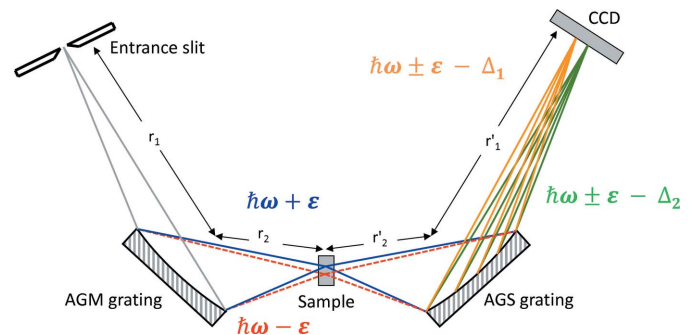

Figure 2
Illustration of the energy-compensation principle of grating dispersion applied to a RIXS measurement. Both gratings have an identical central groove density and the same distance to the sample. After passing through the entrance slit, X-rays of varied energy $\hbar\omega \pm \varepsilon$ are dispersed onto the sample and experience inelastic scattering. Scattered X-rays of identical energy loss (Δ_1 or Δ_2) are dispersed and focused to the same point on the CCD.

optical arrangement identical to the reverse of that of the AGM. If two X-rays with a small wavelength deviation $\Delta\lambda'$ are emitted in reverse from the detector into the AGS with incident angle α', dispersion angle β' and diffraction order k', the dispersion change $\Delta y'$ at the sample would be $(k'r_2'n_0'/\cos\beta')\Delta\lambda'$, in which r_1' and r_2' are, respectively, the entrance arm and the exit arm of the AGS of groove density n_0' at the grating centre; $\Delta\lambda'$ is the deviation in wavelength. If $n_0 = n_0'$ and $r_2 = r_2'$, X-rays elastically scattered by the sample thus become dispersed by the AGS onto the detector with $\alpha' = \alpha$ and $\beta' = \beta$. If the incident X-rays are inelastically scattered by the sample with a constant energy change, the scattered X-rays are also dispersed by the AGS but with a constant shift in α'. This concept constitutes the energy-compensation principle of grating dispersion. The AGM–AGS scheme has two important features: the energy-loss spectra are measured through the superposition of the inelastic X-ray scattering excited with incident X-rays of different energies within the bandwidth of the AGM, and the measurement efficiency is proportional to that energy bandwidth. For IXS measurements in which the energy-loss spectrum does not depend on the energy of incident X-rays, the measurement efficiency is greatly enhanced because of the superposition of inelastic X-ray scattering.

The AGM–AGS scheme requires that $r_2 = r_2'$ and identical n_0 of both AGM and AGS. To achieve the best performance of the AGM, we used the following approach to decide grating parameter n_1. For two X-rays of wavelengths λ_0 and λ_1 within a small dispersion bandwidth and with an identical incident angle α, these X-rays are dispersed and focused to image points B and B_1 corresponding to $r_{2,0}$ and $r_{2,1}$ with dispersion angles β_0 and β_1, respectively. For given n_1 and λ_0, one directly obtains a_2 from equation (4) as follows,

$$a_2 = \left[\left(\frac{\cos^2\alpha}{r_1}\right)(\lambda_1 - \lambda_0) + \left(\frac{\cos^2\beta_0}{r_{2,0}}\lambda_1 - \frac{\cos^2\beta_1}{r_{2,1}}\lambda_0\right)\right]$$
$$\Big/ 2\big[(\cos\alpha + \cos\beta_0)\lambda_1 - (\cos\alpha + \cos\beta_1)\lambda_0\big]. \quad (5)$$

We then obtain $r_{2,0}$ and $r_{2,1}$ and their deviations $\Delta r_2 \equiv r_{2,0} - r_{2,1}$ from (4) and (5). The ideal AGM working condition

Table 1
Optical parameters of AGM and AGS gratings.

Both gratings have a laminar groove profile with duty ratio 0.4:0.6 and groove depth 7 nm.

	AGM	AGS
Size (L × W × T) (mm)	$220 \times 50 \times 10$	$220 \times 50 \times 10$
Coating	Au	Au
Substrate	Si	Si
Curvature (m)	80–120	40–50
Entrance arm (m)	$r_1 = 3.5$	$r_2' = 2.5$
Exit arm (m)	$r_2 = 2.5$	$r_1' = 3.5$
n_0 (grooves mm^{-1})	1200	1200
n_1 (grooves mm^{-2})	0.80	-0.05

is $\Delta r_2 = 0$; under such a condition, the VLS grating focuses the incident X-ray beams on a plane almost perpendicular to the optical axis, rather than on an inclined curved surface, thus matching the sample geometry and satisfying the energy-compensation condition. With $n_0 = 1200$ grooves mm^{-1} and bandwidth 3 eV, we compared Δr_2 of various n_1 and found an optimized $n_1 = 0.80$ grooves mm^{-2} for the AGM such that Δr_2 is between -0.9 mm and 0.1 mm in the energy range from 400 to 1200 eV. Adopting the same approach to analyze the AGS parameters, we obtained an optimized $n_1' = -0.05$ grooves mm^{-2}.

2.3. Optical layout

Fig. 3 illustrates the optical layout of the AGM–AGS beamline. The first optical element is a horizontal focusing mirror (HFM) located at distance 12.05 m from the centre of an elliptically polarized undulator (EPU). A vertical focusing mirror (VFM) is located at distance 1.4 m from the HFM to focus the X-ray beam onto an entrance slit. The light is further focused and dispersed onto the sample by the AGM. An aperture is placed just before the sample to define the energy spread of the incident photons. After the sample, a horizontal refocusing mirror (HRFM) enhances the efficiency of collection of scattered X-rays in the horizontal direction. An AGS is used also to disperse and to focus the scattered light onto a two-dimensional charge-coupled device (CCD). Table 1 lists the parameters of the monochromator and the spectrometer.

2.4. Simulation of spectral resolution

Based on ray-tracing code *SHADOW3* (Sanchez del Rio *et al.*, 2011), we adopted a special ray-tracing scheme that handles simultaneously X-rays of multiple energies from multiple source points to simulate the AGM–AGS instrumental lineshape. The simulations include three steps: (i), (ii) optimizing the AGM and the AGS parameters, and (iii) constructing the instrumental lineshape in energy loss. X-rays of energy 850 eV from a rectangular entrance slit of height 2 µm
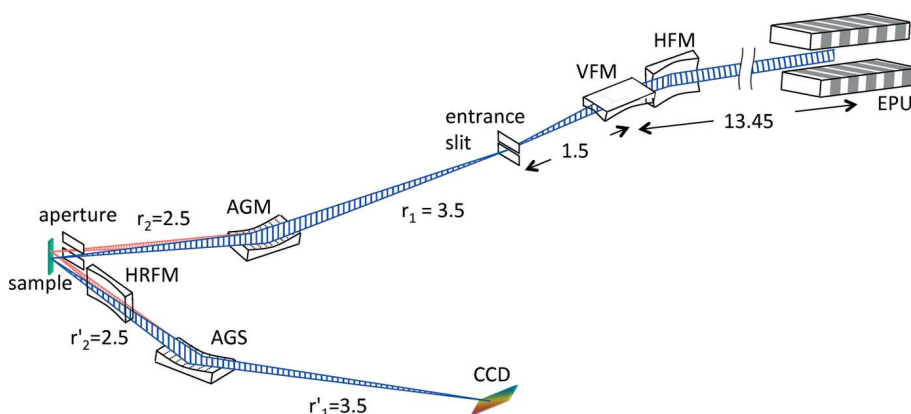

Figure 3
Optical layout of the AGM–AGS beamline and spectrometer. The X-ray source is an elliptically polarized undulator. All distances have units of metres. See the text for the abbreviations of optical elements.
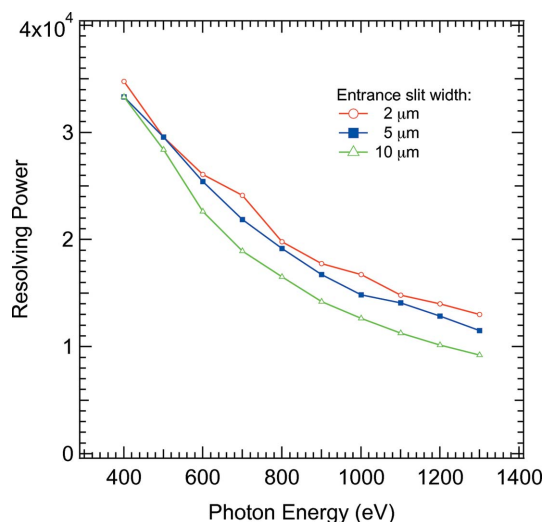
Figure 4
Simulations of the resolving power of the AGM for the entrance slit widths of 2, 5 and 10 μm and the exit width of 3 μm. The resolving power is defined as $E/\Delta E$, where E is the photon energy and ΔE is the energy resolution. All simulations were performed with $\alpha - \beta = 174°$, $r_1 = 3.5$ m, $r_2 = 2.5$ m, $n_0 = 1200$ grooves mm^{-1}, $n_1 = 0.8$ grooves mm^{-2} and slope error = 0.25 μrad r.m.s.

and width 100 μm were focused onto the sample through the AGM grating. The vertical and horizontal divergences of the source were ±0.4 mrad and ±50 μrad, respectively. The corresponding footprint on the AGM grating was 80 mm along the propagation direction. The best parameters of the AGM were obtained on minimizing the spot size on the sample.

We simulated the resolving power of the AGM as presented in Fig. 4; the opening of the sample aperture was 3 μm which does not result in the spectral broadening of the energy-loss spectra measured using the AGM–AGS scheme. The AGM resolving power exceeded 16000 and 12000 for the entire energy range below 1 keV, when the opening of the entrance slits were set to 2 and 10 μm, respectively. The corresponding energy resolutions at 850 eV are 53 and 70 meV. The total energy resolutions in the AGM–AGS set-up are around $\sqrt{2}$ times those of the AGM. The second step was to establish the working parameters of the AGS grating. For a given energy loss, for example 1 eV, the AGS parameters were optimized on minimizing the spot size of X-rays of energy 849 eV on the detector. In the final step of constructing the AGM–AGS instrumental lineshape, the slope error of both gratings was set to 0.25 μrad r.m.s. The energy of the excitation beams was set by apertures of width 2 μm, 10 μm and 100 μm at the sample for varied bandwidths. To mimic inelastic scattering, the energy of scattered X-rays was shifted by the value of the energy loss, and the beam divergence was redefined to meet the AGS acceptance.

Fig. 5 shows the simulated instrumental lineshape of the AGM–AGS design with a slope error of 0.25 μrad r.m.s. In this simulation the energy of incident photons was set to 850 eV; the lineshape of ten inelastically scattered X-ray beams corresponding to energy losses from 0.2 to 2 eV with energy step 0.2 eV were simulated. The width of the entrance slit was set to 10 μm; that of the sample aperture was chosen to be
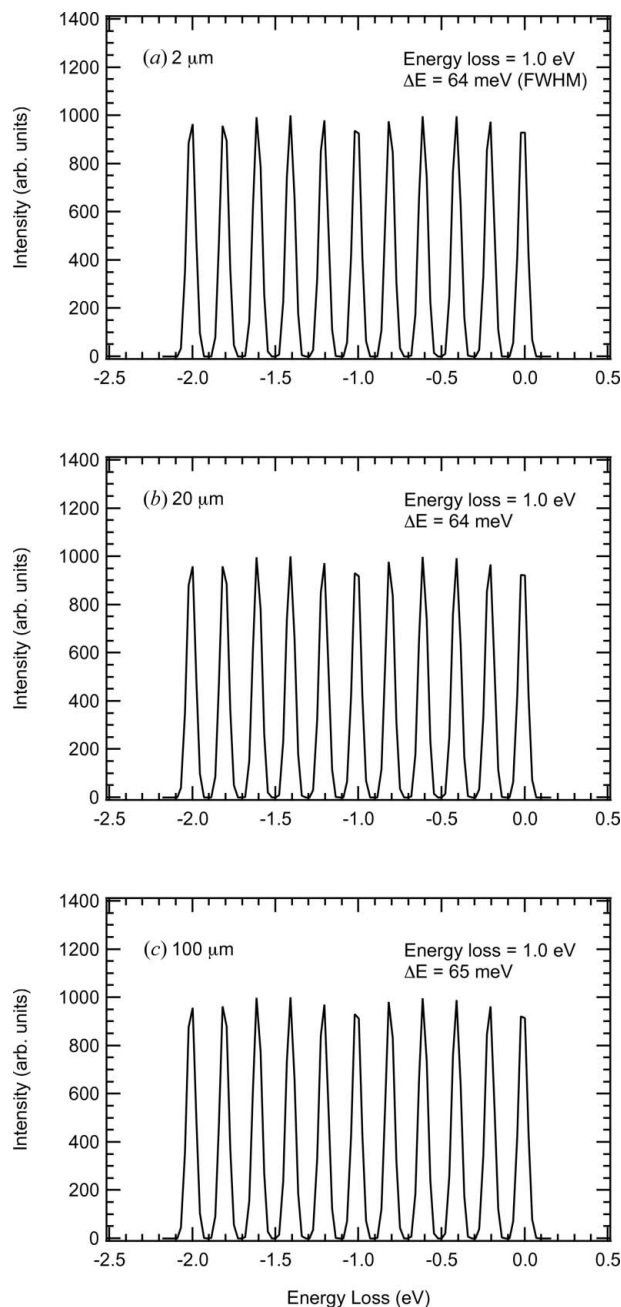

Figure 5
Simulated instrumental lineshapes of ten inelastically scattered X-ray beams of the AGM–AGS beamline and spectrometer corresponding to energy losses from 0.2 to 2 eV with energy step 0.2 eV. The energy of incident photons was set to 850 eV. The opening of the entrance slit was set to 10 μm, that of the sample aperture was (a) 2, (b) 20 and (c) 100 μm. The optimal resolution was set at energy loss 1 eV; the slope error of the active gratings was 0.25 μrad r.m.s. Other optical parameters are described in the text.

2, 20 and 100 μm, corresponding to energy bandwidths of ±25 meV, ±132 meV and ±670 meV, respectively. The instrumental lineshape is insensitive to the opening of the sample aperture; the FWHM at energy loss 1 eV for these settings is ∼64 meV, i.e. a total resolving power ∼13200. For high-resolution IXS measurements, one can decrease the opening of the entrance slit and reduce the slope error of the grating to enhance the resolving power. For example, if the

effect of the slope error of the grating is neglected, the simulated total resolution was 30 meV, a resolving power near 28300, for an entrance slit of width 2 µm and a sample aperture of opening 20 µm. This high-resolution region covers several eV. Even with the slightly uncompensated optical path at both 0 eV and 2 eV, the spectral linewidths remained almost unchanged.

3. Implementing high-resolution RIXS

3.1. Construction of the AGM–AGS system

To test the energy-compensation principle for RIXS experiments, we constructed an AGM–AGS set-up using a side branch of beamline 05 of the Taiwan Light Source (TLS) at the NSRRC. Fig. 6 shows a photograph of the test AGM–AGS beamline and spectrometer. An EPU provided X-rays in an energy range from 400 eV to 1200 eV. The vertical FWHM beam size of electrons at the undulator centre was 63 µm. The front-end of the beamline, which is shown in neither Fig. 3 nor Fig. 6, includes a photon absorber, to protect all components downstream from radiation damage, and two water-cooled apertures, to collimate the X-rays. The front-end apertures are made of OFHC Cu to eliminate unwanted synchrotron radiation from the central cone and most heat. After the front-end, a horizontal focusing mirror focuses the beam in the horizontal direction to be 600 µm at the sample. A vertical focusing mirror focuses X-rays in the vertical direction to be 15 µm at the entrance slit that was set to 10 µm for all test measurements.

An active grating is a key component of the AGM–AGS design. The grating dispersion in both the monochromator and spectrometer conforms to a geometry of fixed in and out directions in which $\alpha - \beta = 174°$. A mechanical bender of clamping type was designed and fabricated to achieve a
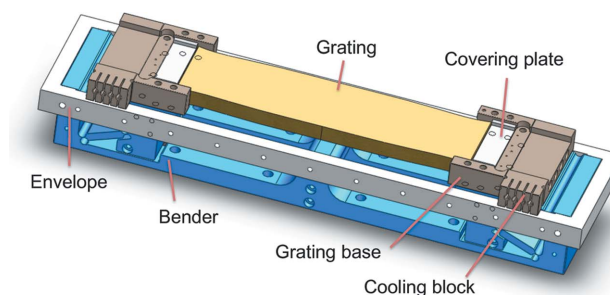

Figure 7
Mechanical drawing of the grating assembly used in the AGM–AGS system. The plane grating is a Si substrate of thickness 10 mm coated with Au. Both ends of the grating are glued to a pair of copper bases and covering stainless-steel plates. Through six M4 screws on both ends, the grating is joined to a flexure-hinge bender made of 17-4 stainless steel. Two piezoelectric actuators are installed underneath the base, allowing us to control the grating profile.

polynomial surface of the grating. The grating assembly includes three major components: a plane grating, a bender and two piezo actuators. The plane grating is made of a Si substrate coated with Au; the thickness of the substrate is 10 mm. The slope error of the flat grating measured with a long-trace-profile device is 0.25 µrad r.m.s. Both ends of the grating were glued to a pair of copper bases and covering stainless-steel plates. With six M4 screws on both ends, the grating was joined to a flexure-hinge bender made of 17-4 stainless steel, allowing the plane grating to be bent to a surface profile of a third-order polynomial with a radius down to 35 m, as illustrated in Fig. 7. The bender was shaped with electric discharge machining to ensure that the central point of the grating surface is stationary within a few micrometres (Chen *et al.*, 2001). Through a strain-gauge feedback, the accuracy of forces applied to both ends of the bender from two high-voltage piezoelectric actuators was within 0.03 N. Simulations using finite-element analysis (FEA) showed that a bent rectangular grating introduces a slope error of 6 µrad r.m.s. We used FEA simulations to obtain a curved shape in the grating width to minimize this effect.

The sample chamber was mounted on a granite support to isolate mechanical vibration, and equipped with kinematic mounts to adjust the chamber position and orientation. A turbo-molecular pump and an oil-free dry pump served to evacuate the chamber initially to a pressure in the 10^{-8} torr range. During an experiment, only an ion pump was used, to diminish mechanical vibration. The top of the chamber contained a sample XYZ-manipulator on a rotation platform with differential pumping. An in-vacuum aperture located before the sample set the bandwidth of the AGM. The aperture is also translatable along the direction of the incident beam. Two knife-edge plates of the aperture were
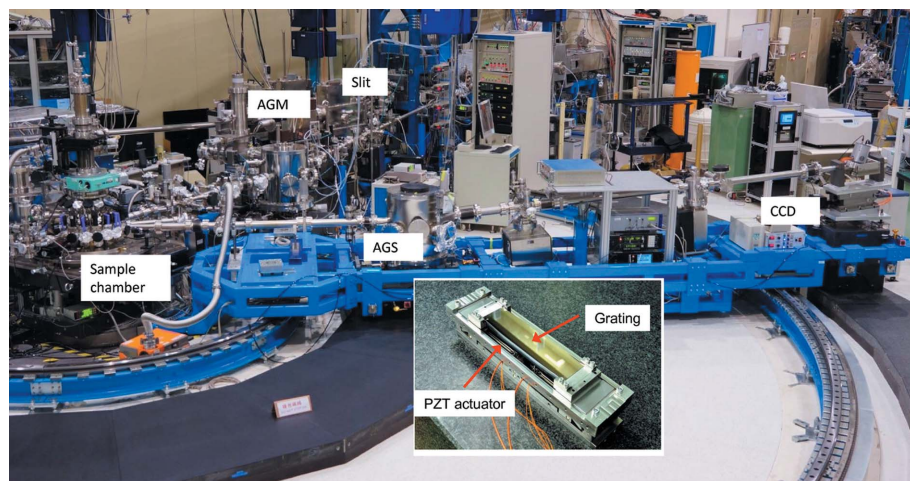

Figure 6
Photographs of the AGM–AGS beamline and spectrometer installed at beamline 05A1 of the Taiwan Light Source. The base granite blocks of the AGS grating and the CCD are separately placed on two granite platforms. Through an air cushion mechanism, the AGS can swing about a vertical axis at the sample position, while the gap between the movable base granite block and the fixed granite platform is between 30 and 35 µm. The rotation range is from 0° to 144°.

installed on a weak-link flexible base to maintain their parallelism. A horizontal refocusing mirror with an incident angle of 2° was installed after the sample to enhance the efficiency of collection of scattered X-rays in the horizontal direction. Measurements of momentum-resolved RIXS require a spectrometer that collects the scattered light emitted from the sample in various directions. A commercial CCD detector (1024 × 1204 pixels, pixel resolution 13.5 μm) collected inelastically scattered X-rays under angle 70° of inclination, *i.e.* the angle between the incident beam and the CCD surface was 20°. The energy range of inelastic excitations that is accessible with our AGM–AGS system is about 15 eV. The AGS grating chamber and the CCD were independently positioned on granite slabs situated separately on two sliding platforms made of granite. Both the AGS grating chamber and the CCD can be lifted 30 μm through an air-cushion mechanism such that the AGS can swing in the scattering plane about a vertical axis passing through the sample.

3.2. Commissioning results

3.2.1. Test of the energy-compensation principle. We used a carbon sample to measure the lineshape of elastically scattered X-rays. Both actuators of AGM and AGS benders were first optimized such that the FWHM of the elastic scattering intensity *versus* energy was minimized. Fig. 8 plots a three-dimensional colour contour of the FWHM of elastic X-rays of energy 870 eV from a carbon sample. With the displacement of one piezo actuator fixed, the optimized working range of the other AGM actuator is 1 μm; the working range of the AGS actuator is 0.5 μm.

After optimizing the working condition for the AGM and AGS, we measured the width of elastic soft X-rays of energy 850 eV from a carbon sample. The inset of Fig. 9 shows plots of scattering intensity *versus* photon energy with varied size of the sample aperture. The best spectral resolution of the test AGM–AGS system was 108 meV for an entrance slit of width
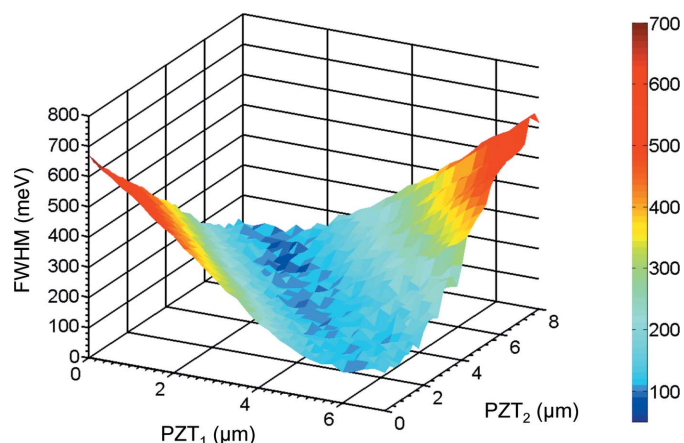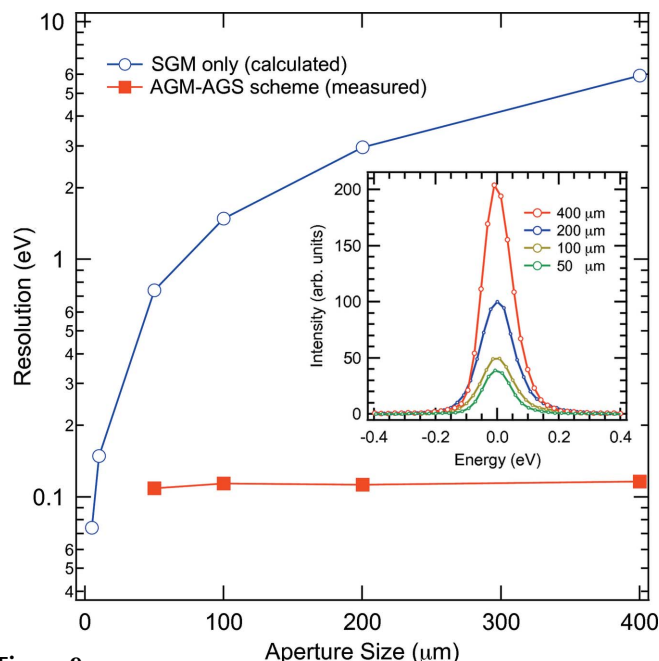

Figure 9
Test of the energy-compensation principle. The FWHM of elastic scattering from a carbon sample is compared with that from a theoretical prediction based on equation (6). Inset: lineshapes of elastic scattering of 850 eV photons from a carbon sample with varied opening of the aperture.

10 μm and a sample aperture of width 50 μm. The measured spectral resolution was insensitive to the aperture opening, as plotted in Fig. 9; the scattered intensity was nearly proportional to the aperture opening, agreeing satisfactorily with a prediction based on the energy-compensation principle. The contribution of the exit slit of width S_2 to the spectral width ΔE_{exit} of a grating monochromator is

$$\Delta E_{\text{exit}} = \frac{E^2}{hc} \frac{S_2\, d \cos \beta}{r_2}, \tag{6}$$

in which E, h, d and c are the photon energy, Planck constant, grating period and speed of light, respectively. Slit opening S_2 is equivalent to the opening of the sample aperture in the AGM–AGS design. Fig. 9 also plots ΔE_{exit} for varied S_2. The spectral resolution of the AGM–AGS scheme arising from the sample aperture has a marked difference from that contributed by the exit slit in a SGM design. In particular, a large sample aperture, *e.g.* 400 μm, does not smear the spectral resolution, in contrast to a SGM design. This prominent feature is helpful to a 'photon-hungry' experiment such as ultrahigh-resolution RIXS. For instance, one can expect a total resolving power of 40000 from a SGM scheme with 2 μm width of both entrance and exit slits for a slope error of grating less than 0.1 μrad r.m.s. Such an ideal design yields a small count rate in a RIXS measurement. Markedly, in the AGM–AGS design, one can increase the opening of the sample aperture to enhance the measurement efficiency without sacrificing the spectral resolution. For example, a sample aperture of 50 μm in the present AGM–AGS design produces a bandwidth of ±350 meV; the collection efficiency is 25 times that of a 2 μm exit slit in a conventional SGM design. This observation leads

Figure 8
Three-dimensional colour contour plot of scattering width for varied displacement of the AGM grating actuators. The scattering width was measured in terms of the FWHM of 870 eV X-rays elastically scattered from a carbon sample. PZT$_1$ and PZT$_2$ are the relative displacements of the two piezo actuators of the AGM grating assembly.

us to conclude that the energy-compensation principle is effective for soft X-ray spectroscopy, and greatly increases the measurement efficiency.

3.2.2. RIXS of NiO. We chose NiO as a test sample for high-resolution RIXS measurements using a side branch of the EPU beamline at the TLS. NiO is a prototypical system of strongly correlated electrons that exhibit many-body characteristic properties. The surface normal of the NiO sample was along the [001] direction; the incident angle was 30° from the sample surface. The scattering angle between the incident and scattered X-rays was 50° as illustrated in Fig. 10(*d*). The inset of Fig. 10(*b*) depicts the X-ray absorption spectrum (XAS) of NiO in the energy range near the Ni L_3 absorption edge. Fig. 10(*a*) plots the colour mapping of RIXS intensity across the L_3 absorption edge, obtained by combining RIXS

Figure 10
RIXS spectra of NiO excited with photon energy varied about the Ni L_3 edge: (*a*) colour mapping of RIXS intensity across the L_3 absorption edge, obtained by combining RIXS spectra excited every 500 meV, (*b*) RIXS spectra excited with incident photons of energies 853, 855 and 857 eV, (*c*) RIXS spectra in an energy range near the elastic scattering excited with of selected incident energies labeled in units of eV, and (*d*) illustration of the scattering geometry. All RIXS spectra were taken at temperature $T = 300$ K. The energy loss is defined as $E_{loss} = E_{out} - E_{in}$, in which E_{in} and E_{out} are, respectively, the energies of incident and scattered X-rays due to inelastic scattering. The energy spacing between successive data points is limited by the CCD pixel size. The inset of (*b*) plots the X-ray absorption spectrum about the Ni L_3-edge.

spectra excited every 500 meV, and Fig. 10(*b*) shows spectra of inelastic soft X-ray scattering measured with varied energy of incident σ-polarized photons that have an *E*-vector perpendicular to the scattering plane. The widths of entrance slit and sample aperture were set to 10 µm and 100 µm, respectively. The photon flux on the sample was 7×10^{11} photons s^{-1} within a bandwidth 1.34 eV. Each RIXS spectrum was recorded for 45 min.

In the ground state of NiO, Ni^{2+} has a $3d^8$ configuration of symmetry $^3A_{2g}$. Beyond the elastic scattering, we observed five Raman-like features in the RIXS spectrum of NiO associated with *d–d* excitations. The *d–d* excitation of least energy is assigned to a triplet–triplet excitation from $^3A_{2g}$ to $^3T_{2g}$ with a two-hole electronic configuration $e_g^\downarrow t_{2g}^\downarrow$ in the final state. The observed excitation energy of 1.027 eV is exactly equal to the crystal field $10Dq$ because one electron is excited from the t_{2g} to e_g orbital without involving a spin flip. The second feature contains excitations of energies 1.65 and 1.75 eV corresponding to transitions to ^1E_g of the two-hole configuration $e_g^{\downarrow\uparrow}$ and to $^3T_{1g}$ of $e_g^\downarrow t_{2g}^\downarrow$. The 1.65 eV transition of $^3A_{2g} \rightarrow {}^1E_g$ is involved with a spin-flip excitation. The third feature at -2.6 eV in the energy-loss spectrum is composed of excitations to singlets $^1T_{2g}(e_g^\downarrow t_{2g}^\uparrow)$ and $^1A_{1g}(e_g^{\downarrow\uparrow})$. The fourth feature between -2.9 and -3.3 eV includes transitions to $^3T_{1g}(t_{2g}^{\downarrow\downarrow})$ and to $^1T_{1g}(e_g^\downarrow t_{2g}^\uparrow)$. The fifth feature at -4.1 eV contains transitions to $^1T_{2g}$ and to ^1E_g.

In addition to *d–d* excitations of NiO, a broad feature of charge-transfer (CT) excitation exists in RIXS spectra excited by incident X-rays of energy greater than 855 eV. For instance, a broad feature centred at energy loss -6 eV was observed in the RIXS spectrum excited by 857 eV photons. This CT excitation appears with a characteristic of constant emission energy, a fluorescent-like feature, as explained below. The ground state of NiO has hybridization between $3d^8$ and $3d^9\underline{L}$ because of charge transfer from the ligand to the cation; $\underline{L}$ denotes a $2p$ hole in the ligand oxygen. Such hybridization produces bonding and antibonding states, in addition to the non-bonding states with a finite width. When the incident photon energy resonates with the transition to the lower edge of the non-bonding states $3d^9\underline{L}$, a CT excitation is enhanced because of the matching of the wavefunctions in the intermediate and final states of RIXS. The CT excitation energy appears to increase with increasing energy of incident photons until it resonates with the upper edge of the non-bonding states corresponding to the CT feature in XAS. Because the bandwidth of oxygen $2p$ states is finite, the RIXS intermediate states and the final states of CT excitations also have finite bandwidths; the CT excitations are hence broad, but these CT excitations arise from RIXS rather than from non-resonant fluorescent emission, as discussed previously (Matsubara *et al.*, 2005; Ghiringhelli *et al.*, 2005).

We also observed spin-flip excitations of NiO. Fig. 10(*c*) shows RIXS spectra in an energy range near the elastic scattering excited with selected incident energies. The data clearly show pronounced energy-loss features at -0.1 and -0.2 eV, corresponding to the magnetic excitations of NiO (de Groot *et al.*, 1998; Ghiringhelli *et al.*, 2009). Our RIXS results which
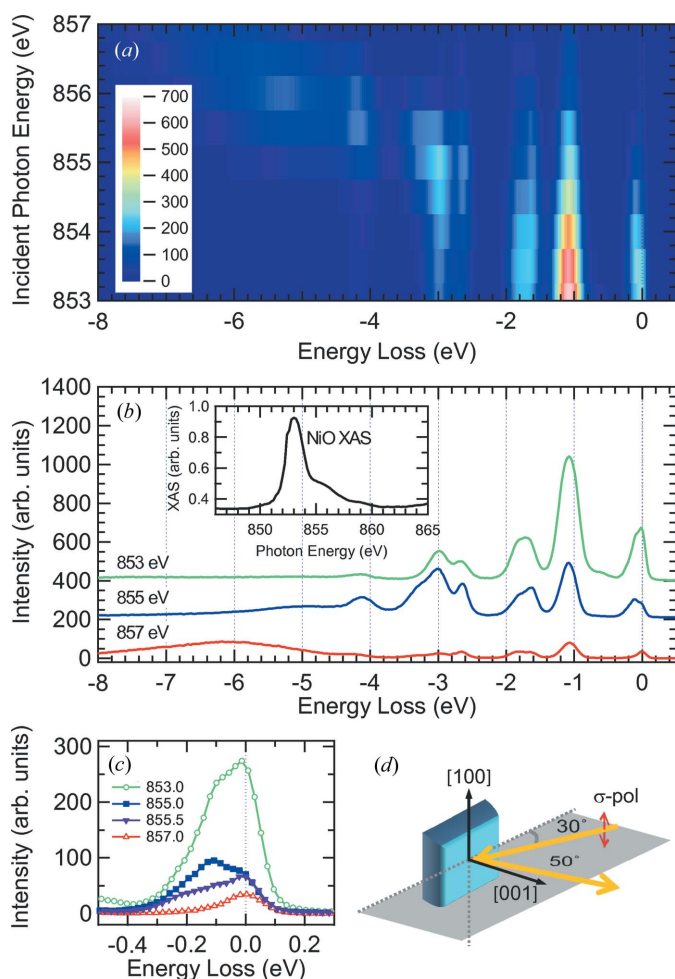
show spin-flip, *d*–*d* and CT excitations are consistent with previous measurements (Ishii *et al.*, 2001; Magnuson *et al.*, 2002; Ghiringhelli *et al.*, 2005, 2009), but the AGM–AGS schemes increased the measurement efficiency. This gain stems from the superposition of the energy-loss spectra excited with incident X-rays within an energy bandwidth, and is particularly useful for obtaining high-resolution non-resonant IXS, in which the energy loss is independent of the incident energy of X-rays and the superposition does not smear the spectral resolution of IXS. In contrast, for a RIXS process, this gain is at the expense of a loss of selectivity of intermediate states. One can still exploit the energy-compensation principle to achieve high-resolution RIXS if the energy bandwidth of the incident X-rays is appropriately selected. For example, the bandwidth in our test RIXS measurement of NiO is 1.34 eV, and the measured RIXS spectra arise from an average RIXS to which a range of intermediate states within this bandwidth contribute. From published RIXS measurements of NiO (Ghiringhelli *et al.*, 2009), we found that the energy-loss feature is rather insensitive to the energy of incident X-rays within this bandwidth. The efficiency gain in our RIXS measurements hence does not result in spectral broadening. Although the bandwidth of the incident X-rays was large, we achieved a total energy resolution of RIXS slightly better than that of data recorded using the ADRESS beamline (Strocov *et al.*, 2010) and SAXES spectrometer (Ghiringhelli *et al.*, 2006).

4. Summary and future improvement

We have experimentally demonstrated an application of the energy-compensation principle of grating dispersion to enhance the efficiency of measurement of inelastically scattered X-rays. The AGM–AGS design has two prominent features: the AGM–AGS scheme ensures that the scattered X-rays of an identical energy loss are dispersed and focused to the same point in the dispersion plane of the spectrometer grating, and a special bendable grating mechanism produces a unique means to diminish effectively the defocus and coma aberrations. Our active grating scheme hence improves greatly the spectral resolution. The commissioning results of RIXS measurements from NiO lead us to conclude that the AGM–AGS scheme is an effective approach to improve the efficiency while maintaining great spectral resolution.

We plan to establish an AGM–AGS system which comprises a polarization analyzer at Taiwan Photon Source, a 3 GeV low-emittance synchrotron light source scheduled to deliver brilliant X-rays to users in 2015. A new horizontal focusing mirror will be installed before the sample to reduce the horizontal beam size on the sample. A long exit arm of the AGS will be used to decrease the limitation of the CCD pixel size and to increase the spectral resolution, because the AGM–AGS design does not require an identical length of the AGM entrance (r_1) and AGS exit arms (r_1'). In the present design, r_1' is 3.5 m; it will be extended to 5 m for an ultrahigh-resolution mode, in the hope of achieving a resolving power greater than 40000 at 900 eV. The construction plan of a new sample chamber is in progress to realise a continuous variation of momentum transfer without breaking the vacuum, allowing us to implement momentum-resolved RIXS measurements.

References

Agaker, M., Andersson, J., Englund, C.-J., Olsson, A., Strom, M. & Nordgren, J. (2009). *Nucl. Instrum. Methods Phys. Res. A*, **601**, 213.

Ament, L. J. P., van Veenendaal, M., Devereaux, T. P., Hill, J. P. & van den Brink, J. (2011). *Rev. Mod. Phys.* **83**, 705.

Chen, S.-J., Chen, C., Perng, S., Kuan, C. K., Tseng, T. & Wang, D. J. (2001). *Nucl. Instrum. Methods Phys. Res. A*, **467–468**, 298.

Fung, H. S., Chen, C. T., Huang, L. J., Chang, C. H., Chung, S. C., Wang, D. J., Tseng, T. C. & Tsang, K. L. (2004). *AIP Conf. Proc.* **705**, 655.

Ghiringhelli, G., Braicovich, L., Schmitt, T. & Strocov, V. (2012). *Synchrotron Radiat. News*, **25**, 16.

Ghiringhelli, G., Matsubara, M., Dallera, C., Fracassi, F., Gusmeroli, R., Piazzalunga, A., Tagliaferri, A., Brookes, N. B., Kotani, A. & Braicovich, L. (2005). *J. Phys. Condens. Matter*, **17**, 5397.

Ghiringhelli, G., Piazzalunga, A., Dallera, C., Schmitt, T., Strocov, V. N., Schlappa, J., Patthey, L., Wang, X., Berger, H. & Grioni, M. (2009). *Phy. Rev. Lett.* **102**, 027401.

Ghiringhelli, G., Piazzalunga, A., Dallera, C., Trezzi, G., Braicovich, L., Schmitt, T., Strocov, V. N., Betemps, R., Patthey, L., Wang, X. & Grioni, M. (2006). *Rev. Sci. Instrum.* **77**, 113108.

Green, P. H., (1999). *Proceedings of the Workshop on Soft X-ray Science in the Next Millennium*, experiments. 15–18 March 2000, Pikeville, Tennessee, USA (http://www.phys.lsu.edu/plummer/downloads/ewp_workshop_X-Ray_Report.pdf).

Groot, F. M. F. de, Kuiper, P. & Sawatzky, G. A. (1998). *Phys. Rev. B*, **57**, 14584.

Harada, Y., Kobayashi, M., Niwa, H., Senba, Y., Ohashi, H., Tokushima, T., Horikawa, Y., Shin, S. & Oshima, M. (2012). *Rev. Sci. Instrum.* **83**, 013116.

Hatsui, T., Setoyama, H., Shigemasa, E. & Kosugi, N. (2005). *J. Electron Spectrosc. Relat. Phenom.* **144**, 1059.

Ichikawa, K., Jouda, K., Tanaka, S., Soda, K., Matsumoto, M., Taguchi, Y., Katsumi, T., Aita, O., Maezawa, H., Azuma, Y. & Kitazawa, H. (1996). *J. Electron Spectrosc. Relat. Phenom.* **78**, 183–186.

Ishii, H., Ishiwata, Y., Educhi, R., Harada, Y., Watanabe, M., Chainani, A. & Shin, S. (2001). *J. Phys. Soc. Jpn*, **70**, 1813.

Kotani, A. & Shin, S. (2001). *Rev. Mod. Phys.* **73**, 203.

Magnuson, M., Butorin, S. M., Agui, A. & Nordgren, J. (2002). *J. Phys. Condens. Matter*, **14**, 3669.

Matsubara, M., Uozumi, T., Kotani, A. & Parlebas, J.-C. (2005). *J. Phys. Soc. Jpn*, **74**, 2052.

Sanchez del Rio, M., Canestrari, N., Jiang, F. & Cerrina, F. (2011). *J. Synchrotron Rad.* **18**, 708–716.

Schlappa, J., Wohlfeld, K., Zhou, K. J., Mourigal, M., Haverkort, M. W., Strocov, V. N., Hozoi, L., Monney, C., Nishimoto, S., Singh, S., Revcolevschi, A., Caux, J.-S., Patthey, L., Ronnow, H. M., van den Brink, J. & Schmitt, T. (2012). *Nature (London)*, **485**, 82.

Schmitt, T., Strocov, V. N., Zhou, K.-J., Schlappa, J. & Monney, C. (2013). *J. Electron Spectrosc. Relat. Phenom.* **188**, 38–46.

Strocov, V. N., Schmitt, T., Flechsig, U., Patthey, L. & Chiuzbăian, G. S. (2011). *J. Synchrotron Rad.* **18**, 134–142.

Strocov, V. N., Schmitt, T., Flechsig, U., Schmidt, T., Imhof, A., Chen, Q., Raabe, J., Betemps, R., Zimoch, D., Krempasky, J., Wang, X., Grioni, M., Piazzalunga, A. & Patthey, L. (2010). *J. Synchrotron Rad.* **17**, 631–643.

Tokushima, T., Harada, Y., Ohashi, H., Senba, Y. & Shin, S. (2006). *Rev. Sci. Instrum.* **77**, 063107.